

RESEARCH ARTICLE

10.1002/2014JB011198

Key Points:

- An approach is introduced to combine micro-xCT imaging with mechanical analysis
- The heterogeneity results in the complexity of the failure of sample
- The compressive strength of the coal is strain rate dependent

Correspondence to:

Y. Zhao,
zhaoyixin_cumtb@hotmail.com

Citation:

Zhao, Y., S. Liu, G.-F. Zhao, D. Elsworth, Y. Jiang, and J. Han (2014), Failure mechanisms in coal: Dependence on strain rate and microstructure, *J. Geophys. Res. Solid Earth*, 119, 6924–6935, doi:10.1002/2014JB011198.

Received 15 APR 2014

Accepted 21 AUG 2014

Accepted article online 23 AUG 2014

Published online 10 SEP 2014

Failure mechanisms in coal: Dependence on strain rate and microstructure

Yixin Zhao^{1,2,3}, Shimin Liu³, Gao-Feng Zhao⁴, Derek Elsworth³, Yaodong Jiang¹, and Jingli Han¹

¹State Key Laboratory of Coal Resources and Safe Mining, China University of Mining and Technology, Beijing, China,

²College of Resources and Safety Engineering, China University of Mining and Technology, Beijing, China, ³Energy and Mineral Engineering, G³ Center and EMS Energy Institute, Pennsylvania State University, University Park, Pennsylvania, USA,

⁴Centre for Infrastructure Engineering and Safety, School of Civil and Environmental Engineering, University of New South Wales, Sydney, New South Wales, Australia

Abstract The brittle coal failure behavior under various axial strain rates from 10^{-3} to 10^{-2} s^{-1} is experimentally and numerically studied. The numerical microscale finite difference model is built on the accurate X-ray microcomputed tomography images, which provides a ground-breaking and bottom-up approach to investigate the effects of microstructure on coal failure under various strain rates. Experimentally, prior to loading, the coal sample is scanned, and the three-dimensional coal structure model is constructed. The microheterogeneous structures are incorporated in the model, which facilitates the deformation and failure mechanism analysis under different loading conditions. The results reveal that the microheterogeneous structures significantly affect the evolution of stress concentrations and deformation behaviors in the sample. The coal tends to fail in the shear mode before the peak strength, since the shear zone is created with high displacements. However, tensile failure ultimately controls the failure process after the peak strength. Notably, the strain rate dependence of coal strength is observed, and an empirical relationship is proposed to describe the dynamic strength of the coal under various loading strain rates. Importantly, the coal strengthens with an increase in strain rate. For brittle material, such as coal, the strength and failure mechanism are strain rate and microstructure dependent. The strain rate-dependent coal strength index (n) is found to be a dynamic parameter in the range of strain rate from 10^{-3} to 10^{-2} s^{-1} , and this finding may extend the concept of strain rate dependence over a broader range of loading conditions.

1. Introduction

Coal is a complex heterogeneous and anisotropic porous medium. Bulk coal consists of three components including organic and inorganic components and voids (pores and fractures) [Karacan, 2007; Yao, 2009]. The spatial distribution of these components controls the microstructure of coals and is determined by the sedimentary and geological history of the coal formation. The complex microstructure of coal results in its response as a discontinuous, inhomogeneous, anisotropic, and nonlinear elastic (DIANE) medium [Hudson and Harrison, 1997]. Coal is a naturally occurring DIANE material. Due to these features, understanding, characterizing, and modeling failure mechanisms for coal subjected to various loading conditions remain challenging, with detailed failure mechanisms incompletely understood [Scholtès *et al.*, 2011; Tsafnat *et al.*, 2008, 2011]. One key question relates to how the microstructure of coal influences the initiation, propagation, and coalescence of microfractures that are ultimately manifest as macrofailure. Thus, characterization of the microstructure of coal is important in understanding macrofailure mechanisms.

Numerous attempts have been made to analyze the impact of microstructure on macroscopic mechanical properties. Medhurst and Brown [1998] used brightness profiles to estimate the microstructure of coal and to correlate these data with uniaxial compression strengths. Esterle *et al.* [1994, 2002] studied the characteristics of coal breakage behavior during mining and crushing, and they were able to predict the size distribution of broken coal following fragmentation. Scholtès *et al.* [2011] investigated the contribution of discontinuities on the strength properties of a generic bituminous coal using discrete element methods. Pan *et al.* [2013] evaluated how coal rank and maceral composition influence the mechanical behavior of coal, noting that uniaxial compressive strength and Young's modulus both increase as coal rank increases. Poulsen and Adhikary [2013] studied the impact of sample size on coal strength and found that the tensile strength of the cleats, fractures, and microcracks in the coal controls the rock mass strength. Moreover, characterization by

Commonwealth Scientific and Industrial Research Organisation for highwall mining pillar design [Medhurst and Brown, 1998; Medhurst, 1996] noted a lack of statistical similarity in coal strength between samples from the same locality. Similar results were obtained by Mark and Barton [1996] based on a review of uniaxial compressive strength (UCS) tests on coal for more than 3200 samples. They also identified a high variability in strength of coal samples from the same seam and with the same size and shape. These foregoing investigations demonstrate that the UCS and failure behaviors of coal are microstructure dependent. However, the relationship between coal microheterogeneity and UCS is not fully understood due to prior inadequate constraints on microstructure. In addition, limited effort has been applied to determine the influence of material heterogeneity on stress redistribution and its impact on coal failure behavior under uniaxial compressive loading.

Apart from the microstructure itself, the strength and failure mechanisms of coal are also affected by the loading rate [Okubo *et al.*, 2006]. Okubo *et al.* [1992], Ishizuka *et al.* [1993], Ray *et al.* [1999], Li and Xia [2000], Kohmura and Inada [2006], Fuenkajorn and Kenkhunthod [2010], and Wang *et al.* [2013] conclude from experimental observations that the uniaxial compressive strength of rock increases with an increase in strain and loading rates. However, it remains unanswered how the combined effects of microheterogeneity and loading/strain rates influence the strength and failure behavior of coal. This study addresses this important issue.

X-ray microcomputed tomography (CT) is a noninvasive and nondestructive imaging technique capable of characterizing the coal cleats/fractures [Karacan and Okandan, 2000; Karacan, 2003; Mazumder *et al.*, 2006; Pyrak-Nolte *et al.*, 1997; Van Geet and Swennen, 2001; Wolf *et al.*, 2008; Yao, 2009], macerals [Van Geet *et al.*, 2001; Verhelst *et al.*, 1996], minerals [Golab *et al.*, 2013; Simons *et al.*, 1997], and gas sorption properties in coal [He *et al.*, 2010; Karacan and Okandan, 2001; Karacan and Mitchell, 2003; Wang *et al.*, 2013]. This technique has also been used to investigate coal drying [Mathews *et al.*, 2011], aperture enhancement in coal [Kumar, 2010], swelling related to CO₂ injection [Karacan, 2007; Pone *et al.*, 2009; Pone *et al.*, 2010], as well as to investigate the features of incipient failure in coal under static and dynamic loading conditions [Zhao and Jiang, 2010; Zhao *et al.*, 2013]. This technique provides new opportunities for microstructure characterization without destruction of the sample.

The digital images obtained by micro-X-ray CT (xCT) are particularly suitable for analysis using numerical modeling techniques for studying the microstructure and properties of porous materials [Garboczi *et al.*, 1999; Olson and Rothman, 1997; Spanne *et al.*, 1994; Tsafnat *et al.*, 2008]. Since the early 2000s, the use of xCT in conjunction with computer simulations has become more popular. Combinations of both techniques can be found in different applications such as the analysis of fluid flow through pore networks [Lin and Miller, 2004; Sukop *et al.*, 2008], the permeability of microstructures [Selomulya *et al.*, 2005; Spanne *et al.*, 1994], the capillary properties of porous media [Karpyn and Piri, 2007; Vogel *et al.*, 2005], the dissolution of tablets [Jia and Williams, 2006, 2007], and granule compression [Golchert *et al.*, 2004]. The combination of xCT with computer simulation also offers the possibility of investigating different physical and industrial problems in an integrated and complementary manner. This is achieved by characterizing structural changes through the use of xCT and in evaluating response through the use of numerical modeling for flow, transport, reaction, and transformation.

In this study, we investigate the effect of microstructure on the failure of coal under five different uniaxial compressive strain rates. Our approach combines micro-xCT imaging with microfinite difference analysis. The numerical modeling is based on Mimics (Materialise Inc., France) and FLAC^{3D} (Itasca Inc., USA). To obtain an accurate geometry of the numerical model, a multiple-threshold segmentation approach is employed. The three-dimensional model is reconstructed manually using Mimics and subsequently input for stress analysis into FLAC^{3D}. Then, a series of numerical simulations are completed to investigate the effect of microstructure on the failure behavior of coal at various strain rates. A unified empirical relationship is proposed to describe the dynamic behavior of the coal relative to strain rate. The results provide a robust interpretation for the variability of coal strength in laboratory compressive tests.

2. Experimental Work and Numerical Model Creation

In this section, we define the form of the sample and its discretization in space to enable the analysis of failure under applied loads. Material characteristics are recovered from the micro-xCT imaging.

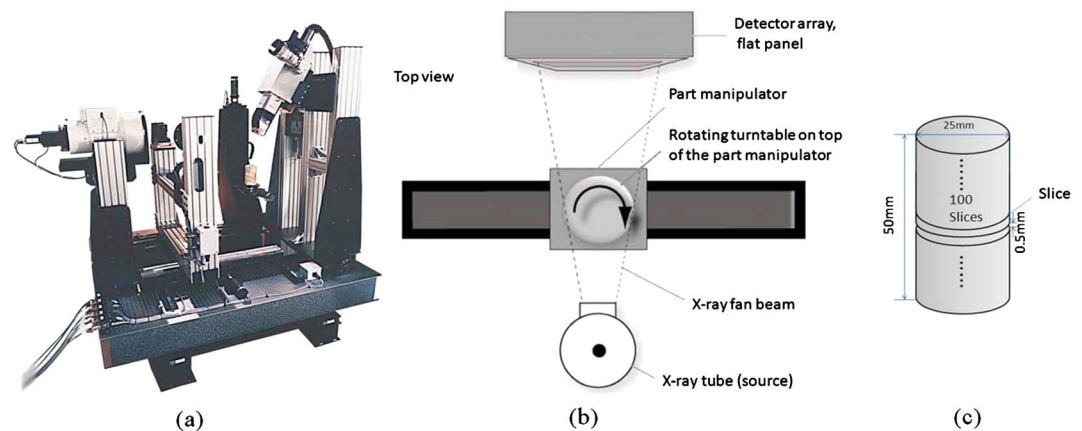


Figure 1. Micro-xCT scanner associated with rock testing system. (a) Diagram of micro-xCT scanning device. (b) Top view of the schematic layout of the scanner. (c) Sample dimensions and scan slice spacing.

2.1. Specimen

A cylindrical core is drilled from a coal block recovered from the No. 9 coal seam in the Tangshan Mine, Kailuan Basin, Hebei Province, China. After the block was removed from the face, it was immediately coated with water-based polycrylic resin to prevent oxidation and drying during transportation. Multiple cores, 25 mm in diameter and 50 mm in length, were then drilled parallel to the bedding plane. The sample was prepared in accordance with the procedures and shape tolerances as outlined in *American Society for Testing and Materials D4543-85* [1985]. The sample comprises coking coal, with vitrinite reflectance (R_o) of 0.9–1.13%, moisture content of (1.84%), ash (27.21%), and volatile matter (33.0%) as determined by the proximate analysis [D5142-09, 2009]. The average maceral composition consists of abundant vitrinite (67.8%), comprising telocollinite (41.7%), telinite (17.7%), desmocollinite (4.9%), and corpocollinite (2.9%). The inertinite group (24.5%) is essentially composed of semifusinite (16.5%), fusinite (3.9%), and inertodetrinite (4.1%). The components of liptinite group are not observed. Mineral matter present in minor proportions (7.7%), comprising dolomite (10.8%) and calcite (9.3%), is defined by X-ray diffraction. The density of the coal is on the order of 1.51 g/cm^3 with moisture content on the order of 1.9%.

2.2. Micro-xCT Scanning

The core sample was scanned using an ACTIS-225FFI micro-xCT scanner manufactured by BIR Corporation, USA, as shown in Figure 1a. The minimum resolution of the scanner is $10 \mu\text{m}$ for an object of 4.8 mm. However, the resolution under the conditions stated here is approximately $30 \times 30 \mu\text{m}^2$ for the scanner operated at 180 Kv and $200 \mu\text{A}$ at a raster of 1024×1024 pixels. The scan time is 9 s per slice with slice thickness and slice spacing both of 0.5 mm. Figures 1b and 1c show the microfocus xCT and the layout of scanned slices in the specimen.

2.3. Uniaxial Compression Test

After xCT scanning, a destructive uniaxial compression test is performed at room temperature using an automated uniaxial loading system that may be completed with the sample within the micro-xCT scanner [Zhao and Zhao, 2011]. The displacement-controlled loading speed of the crosshead is set at 0.05 mm/s , which gives strain rate of 0.001 s^{-1} . The complete stress-strain curve is recorded for the full loading cycle with the strength of sample of 7.6 MPa. Figure 2 shows the experimental results for the static mechanical test. Figure 2a shows the testing system, and Figures 2b and 2c show the sample postfailure. Figure 2d shows the complete stress-strain curve of the sample with the digital radiography at various stress levels.

2.4. Creation of Finite Difference Model Geometry From xCT Images

Since the gray scale of individual voxels in the xCT image is a direct indication of the material density, it can be used as threshold to distinguish the image into multiple sections of material density. The coal normally

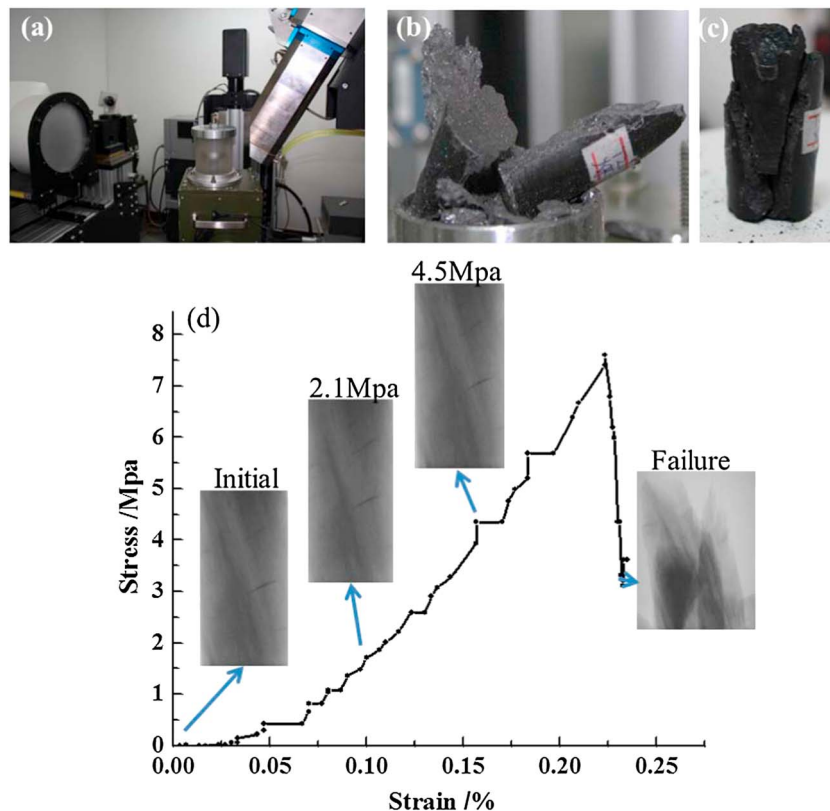


Figure 2. Static uniaxial compression test system and the results of stress-strain curve with the digital radiographies. (a) Diagram of uniaxial rock loading system and micro-xCT scanner. (b) The postfailure sample. (c) The reassembled rock core with main broken pieces. (d) The stress-strain curve with the digital radiographies at the different compression stresses as well as at the postfailure stage.

comprises three basic components, i.e., the voids, coal matrix, and minerals. A three-dimensional (3-D) coal sample with microstructures can be reconstructed by systematically stacking a series of two-dimensional (2-D) X-ray images. In this study, a total of 100 scanned 2-D X-ray images of the coal sample are stacked using the Mimics software and a 3-D sample with the microstructural information reconstructed as shown in Figures 3a and 3b. In Figure 3b, the bright white represents the minerals that have a higher CT number relating to higher density. The gray typically represents the organic coal matrix. During the image processing, the uniform gray scale thresholds were universally applied to each slice.

For the Mimics program, material groups with different properties are assigned based on the gray values in the micro-xCT images. The 3-D model comprising different groups is generated as shown in Figure 3c. The 3-D reconstructed model is then meshed for the solid and internal pores. Surface meshes are then transformed from triangular elements wrapping the solid model and the pore boundaries [Tsafnat *et al.*, 2008]. Based on the optimized surface meshes, the mapping algorithm is adopted to generate meshes comprising four-node tetrahedral elements. The number and quality of the tetrahedral elements are controlled by the mesh size during generation of the volume-filling meshes. In these particular models, the total number of elements and nodes were 770,895 and 124,302, respectively. The 3-D model is then exported to ANSYS (ANSYS Inc., Canonsburg, USA) for mesh confirmation and resolution and then to FLAC^{3D} to allow stress analysis. Figures 3d and 3e show the constructed 3-D model and element mesh in FLAC^{3D}.

2.5. Estimation of Material Properties

In our simulations, three different components are modeled in the bulk coal: pores and fractures, coal matrix, and mineral inclusions. The mineral inclusions are much denser than the coal matrix, and thus, these two

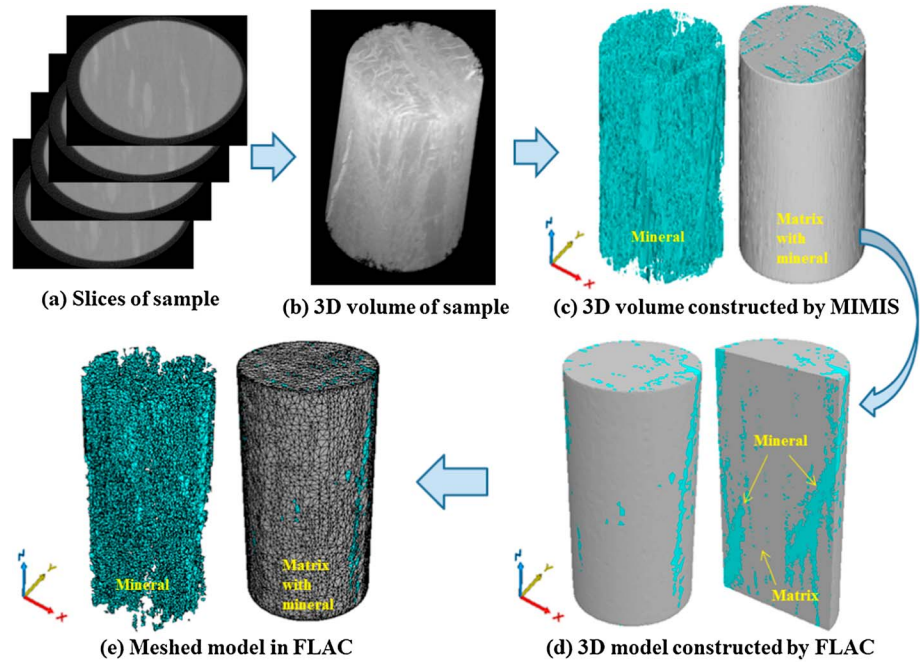


Figure 3. The 3-D representative microstructure photo achieved by micro-xCT scanner and modeling process. (a and b) Representative 3-D microstructure of the specimen shows the mineral inclusion distribution. (c) The 3-D models of mineral inclusion and coal matrix reconstructed by Mimics (inclusion is shown at the left). (d and e) The 3-D element meshed models constructed by FLAC^{3D}. From left to right, the models are meshed inclusion, meshed body including coal matrix and mineral inclusion, 3-D model, and vertical cross section of FLAC^{3D} model before being meshed.

materials are easily differentiated. The pores and fractures are both void space and are automatically represented in the model. To obtain the mechanical properties for the coal matrix and mineral inclusions, microindentation tests are performed [Mahabadi et al., 2012; Randall et al., 2009]. Microindentation is performed by an MH-6 microindentation tester with a Vickers indenter on a 10 mm thick polished section of the coal. Five indentation points are selected and tested in the coal matrix and the mineral inclusion region. The indentation tests are completed under load control—the maximum indentation load is 918 mN. A pause of 5 s was applied at maximum load during which the load was retained constant. During the indentation tests, the hardness of the coal matrix and mineral inclusions are recorded with the results given in Table 1. The indentation hardness of the material correlates with its mechanical properties, and the relationship has been quantitatively reported by Wang et al. [2003]. Based on this relationship, the Young’s modulus (E) and Poisson’s ratio (ν) of the coal matrix were estimated to be 4 GPa and 0.33, respectively. Similarly, the E and ν of the mineral inclusions were estimated to be 35 GPa and 0.14. We note that the application of indentation tests to characterize geomaterials has certain disadvantages—these include the difficulty in measuring intergranular properties, uncertainty in locating single grains by microscopy, and that the sample surface cannot be easily polished flat at the scale of microns [Mahabadi et al., 2012; Randall et al., 2009]. Due to these limitations, the resulting material mechanical properties contain innate uncertainties. Moreover, isotropic elastic properties of the coal matrix and mineral inclusions are assumed. The constitutive model for the inclusions is set as a Mohr–Coulomb model, but strain softening is assumed for the coal matrix. In the latter model, the cohesion, friction, dilation, and tensile strength may soften after the onset of plastic yield by a

	Indentation Hardness(kg/mm ²)					Average(kg/mm ²)
	1	2	3	4	5	
Coal matrix	29.3	35.8	28.1	36.6	35.3	33.02
Inclusion	209.3	157.0	208.3	161.0	155.7	178.26

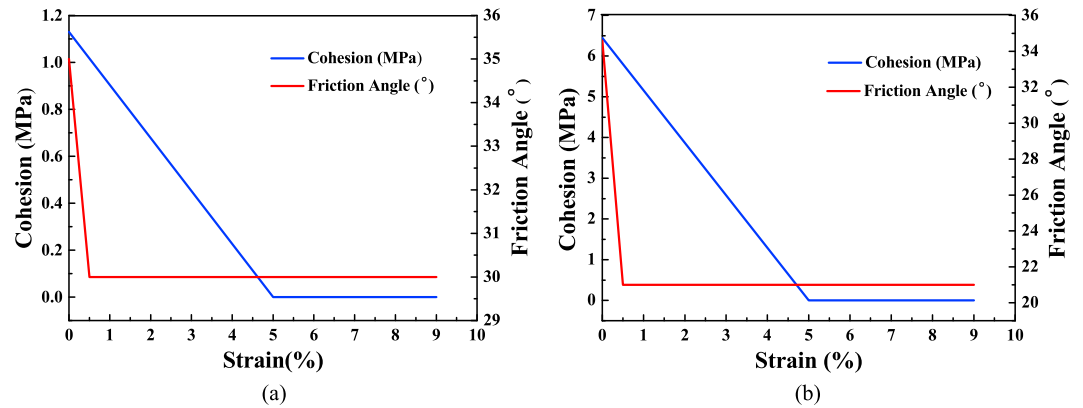


Figure 4. Variation of cohesion and friction angle with plastic strain applied in the simulation model. (a) Model for coal matrix. (b) Model for mineral inclusion.

user-defined and piecewise linear function, as shown in Figure 4. The mechanical parameters used in the simulation are listed in Table 2.

2.6. Uniaxial Loading and Boundary Conditions

The nodes at the top and base of the mesh are laterally constrained due to friction. All side nodes displace freely under the uniaxial compressive condition with no lateral confinement. In order to analyze the impact of deformation rate on the UCS and failure behavior, the top and bottom nodes are assigned five compressive displacement rates of 0.25×10^{-6} , 0.5×10^{-6} , 2.5×10^{-6} , 5×10^{-6} , and 10×10^{-6} mm/step. Here the “step” is the time step in the simulation.

2.7. Numerical Simulation

Uniaxial compression tests are extensively used to estimate UCS and to characterize the failure behavior of rock. In this work, the microheterogeneity of the sample is used to capture the complete process of micro/macrofracture initiation, propagation, and coalescence and hence to investigate the fracture-induced progressive failure of rock. The unique feature of our numerical study is that the geometry of the model is constructed based on the “real” microstructure recovered from 3-D micro-xCT images. Thus, the model truly represents the distributions of mineral inclusions, pores/cleats, and the coal matrix. The model is then used to characterize the failure behavior of coal under compressive loading. Based on the numerical analysis, the stress distribution, localized normal and shear strain rates, and the localized plastic region can be characterized and mapped under various conditions of uniaxial compression and deformation rates. The results inform the mechanisms of failure and the role of microstructure and inclusions and deformation rates on that behavior. An improved understanding of coal failure enables an improved evaluation of the stability of underground structures in coal, e.g., roof and ground control and the design of pillars, to prevent mining-induced safety hazards such as coal/rock bursts and roof falls.

3. Results Analysis and Discussions

Figure 5 presents the full stress-strain curves for the coal samples under the applied distribution of deformation rates. These localized stress concentrations are not uniformly distributed across the sample and vary with location due to the effects of structural microheterogeneity. It is apparent that axial stress

Table 2. Mechanical Parameters Used in the Simulation

Property	Young's Modulus (GPa)	Poisson's Ratio	Tensile Strength (MPa)	Cohesion		Friction Angle	
				Original Value (MPa)	Residual Value (MPa)	Original Value (Degree)	Residual Value (Degree)
Inclusion	35	0.14	3.34	6.45	6.45E-6	34.6	21
Coal matrix	4	0.33	0.20	1.13	0.113	35	30

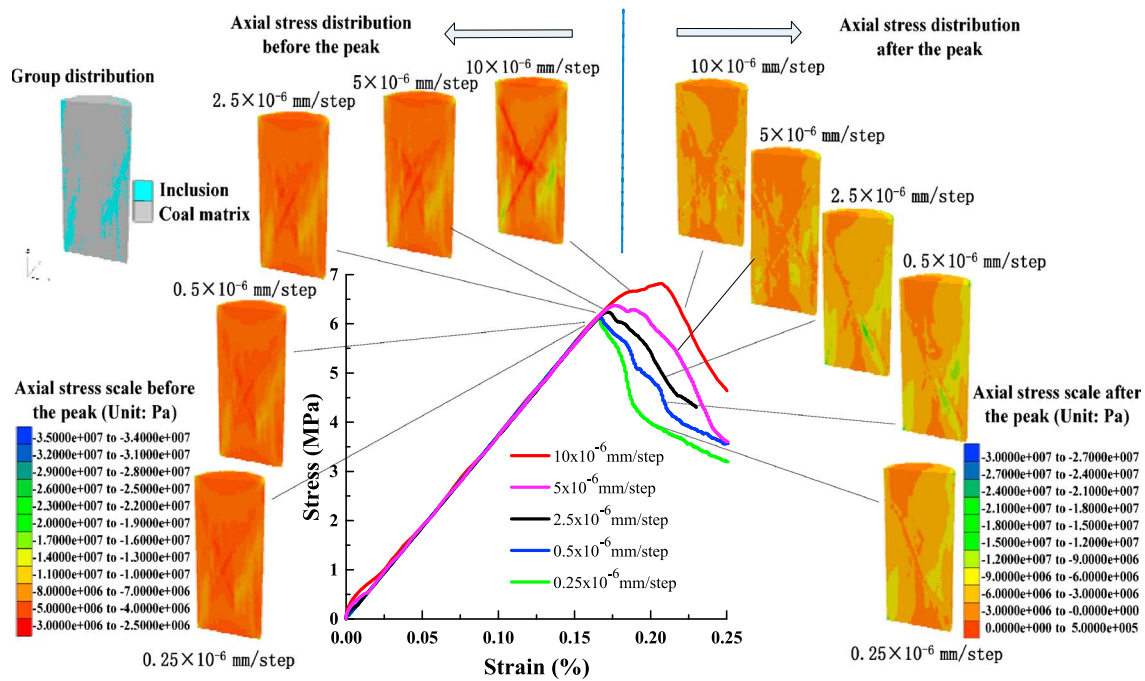


Figure 5. Stress-strain curves for the coal samples under the applied distribution of deformation rates with the axial stress distribution before and after the peak stress.

concentrations are lower on the coal matrix and higher on the mineral inclusions within the sample prepeak strength. Based on the simulation results, the higher the deformation rate, the more heterogeneous the stress distribution. For example, a relatively high stress concentration develops when the deformation rate is 10×10^{-6} mm/step within the mineral inclusions as shown in Figure 5. At postfailure stage, the stress release and the distribution of the stress-released region become more complex with an increase in the deformation rate. However, the inclusion still exhibits higher residual stress than that in the coal matrix. This heterogeneity in stress is due to the microscale heterogeneity of the sample.

Figure 6 shows the accumulated distribution of failed (plastic) elements in the sample at the peak stress, representing macroscopic failure for various deformation rates. The failure features of the sample are indicated by the plastic elements in the model. In Figure 6, the left five images display the simulated element status within the sample before the peak stress at deformation rates of 0.25×10^{-6} , 0.5×10^{-6} , 2.5×10^{-6} , 5×10^{-6} , and 10×10^{-6} mm/step, respectively. It is apparent that the failure of the elements is dominated immediately by shear prepeak strength. Moreover, the distribution of the plastic elements is affected by the distribution of mineral inclusions—the majority of the inclusion elements are elastic at peak strength. With an increase of the deformation rate, more and more plastic failure elements develop at the periphery of the coal matrix and the inclusion. The right five images of Figure 6 show the evolving failure of elements in the sample postfailure. Tensile failure dominates the failure behavior, although a shear zone ultimately develops across the inclusions—the inclusions acting as strain and failure nuclei. A greater number of mineral inclusion elements fail in tension as the deformation rate increases. To some extent, the mineral inclusions serve as a skeletal framework to provide additional support to the sample in compressive loading. However, the random distribution of the inclusions results in the ultimate complexity of failure in the sample.

Figure 7 shows the shear strain rate in the sample both before and after the peak. At prepeak stage, conjugate shear zones develop in the center of the sample. At the postfailure stage, the zones of elevated shear strain traverse and dissect the sample. The shear strain zone is more complex with an increase in the deformation rate before peak strength. However, at the postfailure stage, the failure occurs mainly along the zone(s) of high shear strain. As Figure 7 shows, the zone of localized shear strain comprises a single incline across the sample when the deformation rate is less than 10×10^{-6} mm/step. Although this

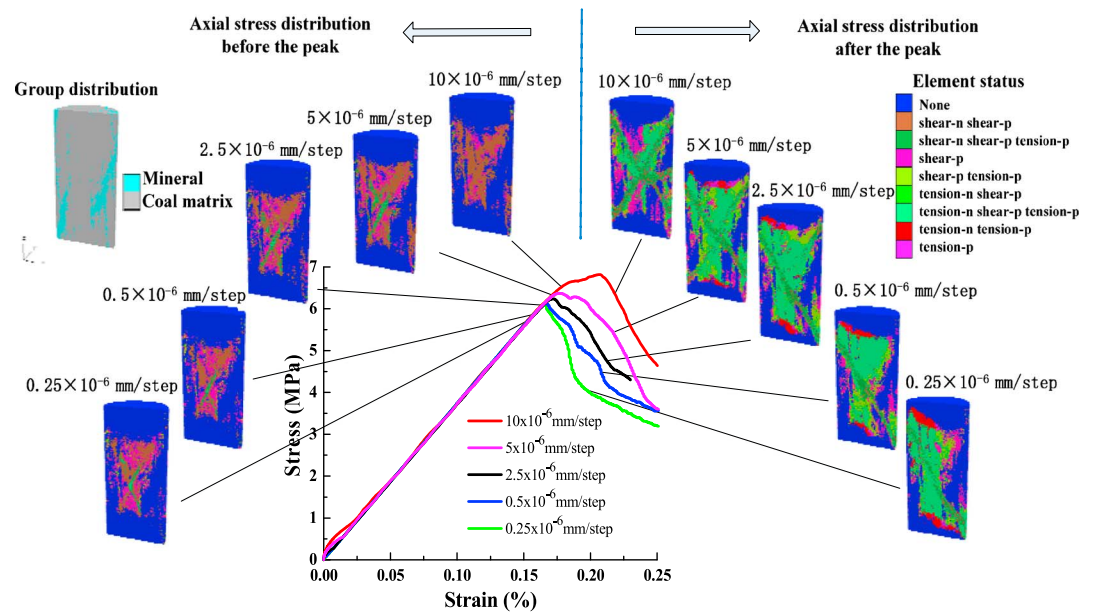


Figure 6. Stress-strain curves for the coal samples and accumulated distribution of failed (plastic) elements in the samples before and after the peak stress for various deformation rates.

zone of enhanced shear strain is indistinct prepeak when the deformation rate reaches 10×10^{-6} mm/step, ultimate failure is more complex. This suggests that the sample fails more suddenly and intensively and in a multimechanistic failure mode [Sleep, 1997] at high deformation rate. This finding is consistent with the field observations.

To show the 3-D localization in the shear strain zone, the main shear strain zones are represented under various deformation rates in two orthogonal directions as shown in Figure 8. The localized zone of shear

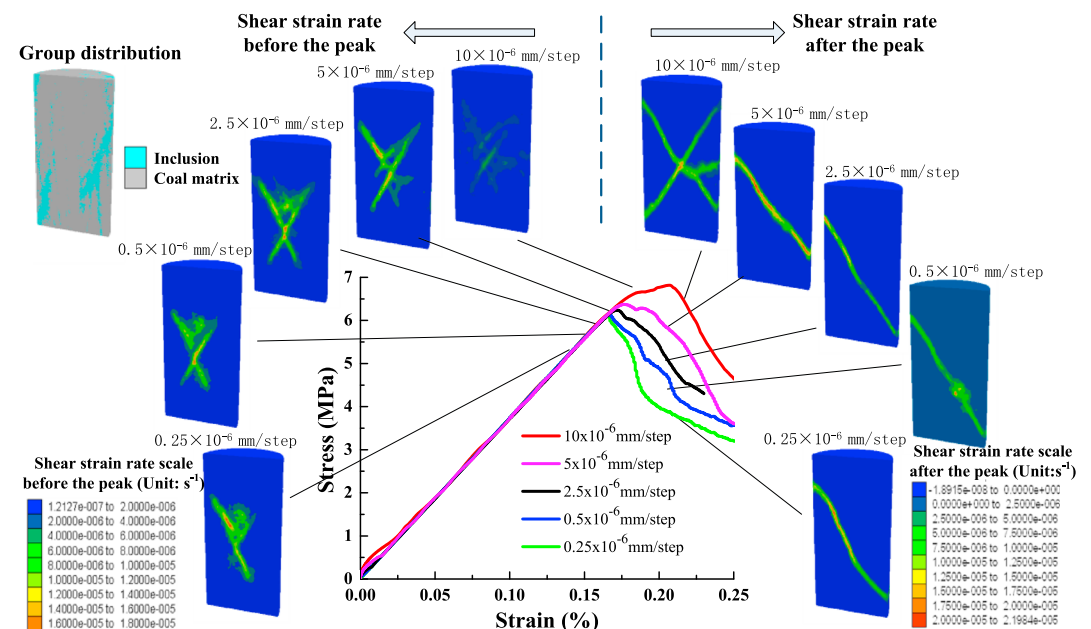


Figure 7. Shear strain rate in the sample both before and after the peak.

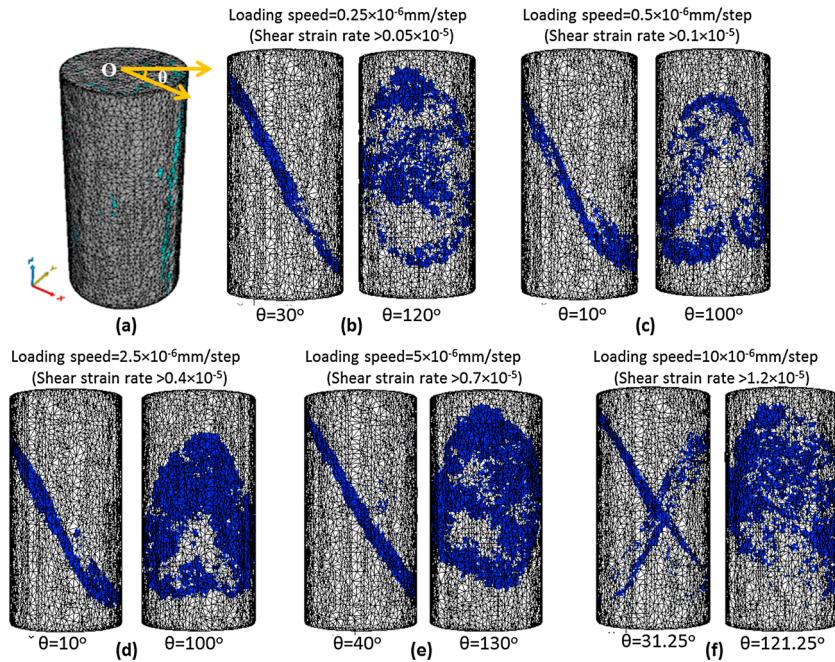


Figure 8. Distribution of localization zones of shear strain rate in the sample under various deformation rates. (a) The diagram of observation direction for the sample. The shear strain rate localization zones in the sample with the deformation rate at (b) 0.25×10^{-6} , (c) 0.5×10^{-6} , (d) 2.5×10^{-6} , (e) 5×10^{-6} , and (f) 10×10^{-6} mm/step, respectively.

strain shows the main failure. The dip angles of these failure surfaces are $\sim 55^\circ$ with trend angles (θ) ranging from 10° to 40° . The inclination of $\sim 55^\circ$ represents a frictional angle (ϕ) on the order of $55^\circ = 45^\circ + \phi/2$ or $\phi \sim 20^\circ$.

As the prescribed time step approaches 5.965×10^{-6} s/step, the strain rate of samples under compressive loading can be calculated. The results for the peak strength of the coal samples at different strain rates, mainly from 10^{-3} to 10^{-2} s $^{-1}$, are shown in Table 3. Many previous attempts have been made to derive empirical equations to express the relationship between the strain rate and rock material strength. For example, Hashiba et al. [2006] proposed an empirical equation to describe the increase of compressive strength of rocks with strain rate as

$$\frac{\sigma_F}{\sigma_s} = \left(\frac{\dot{\epsilon}_F}{\dot{\epsilon}_s} \right)^{\frac{1}{1+n}} \tag{1}$$

where σ_F is the peak strength at strain rate $\dot{\epsilon}_F$ and σ_s is the peak strength at strain rate $\dot{\epsilon}_s$. Parameter n is the strain rate dependence, considered an essential parameter characterizing rock strength and the time dependency of deformation. However, this equation represents a specific range of strain rates and for particular materials and so may be not suited to describe the essential features of strain rate dependence for a broad range of strain rates and different materials. Moreover, prominent strength fluctuations have been observed in rock material for the range of strain rates from 10^{-3} to 10^{-1} s $^{-1}$ [Gong and Zhao, 2013].

Deformation Rate (mm/Step)	Strain Rate (s $^{-1}$)	Peak Strength(MPa)	Strain Value as Peak Strength (%)
0.25×10^{-6} mm/step	0.00167	6.099	0.166
0.5×10^{-6} mm/step	0.00334	6.125	0.167
2.5×10^{-6} mm/step	0.0167	6.237	0.172
5×10^{-6} mm/step	0.0334	6.371	0.177
10×10^{-6} mm/step	0.0668	6.817	0.207

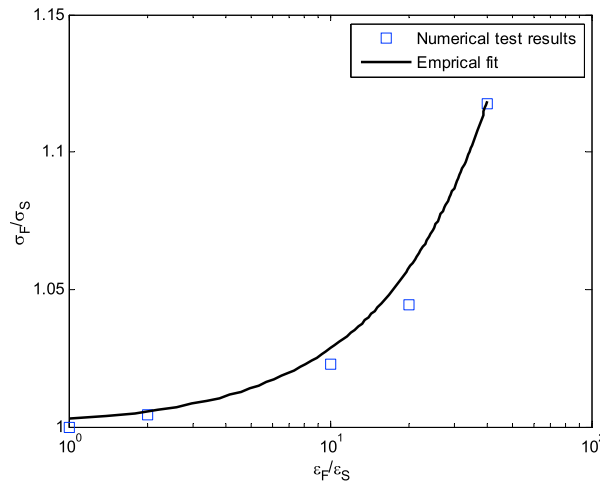


Figure 9. Simulation results and the empirical equation relating the σ_F/σ_S and the ratio of strain rate ϵ_F/ϵ_S .

Such strength fluctuations are also observed in our simulation results (see Table 3 and Figure 9). Thus, equation (1) is no longer applicable. In order to describe the dynamic strength behavior of the coal for a wider range of strain rates, the following empirical relationship is fit to the numerical results:

$$\frac{\sigma_F}{\sigma_S} = e^{\alpha\left(\frac{\dot{\epsilon}_F}{\dot{\epsilon}_S}\right)} \quad (2)$$

where α is a parameter to describe the dynamic strength behavior over a wide-range strain rates and is fit to $\alpha \sim 0.0028$. Compared with equation (1), the relationship between n and α is given as

$$n = \frac{\ln\left(\frac{\dot{\epsilon}_F}{\dot{\epsilon}_S}\right) - \alpha\left(\frac{\dot{\epsilon}_F}{\dot{\epsilon}_S}\right)}{\alpha\left(\frac{\dot{\epsilon}_F}{\dot{\epsilon}_S}\right)} \quad (3)$$

Based on equation (3), n is not a constant and varies with strain rate. This finding conflicts with previous results [e.g., Okubo et al., 2006; Hashiba et al., 2006], which indicate that n is a constant and depends on material properties. This may be attributed to the wider range of strain rate we apply.

It is also worth noting that a preliminary attempt at 3-D finite difference modeling using the micro-xCT data revealed the impact of heterogeneity on the failure of the core sample. In prior investigations, statistical approaches have been employed to describe the heterogeneity of material parameters in rocks including the use of Weibull distribution functions [Fang and Harrison, 2002; Feng et al., 2006; Ma et al., 2011; Tang et al., 2000]. Compared to statistical approaches, the method applied in this investigation permits a better understanding of the effect of realistic microstructure on the failure process and integrates the true material microheterogeneity into the strength and failure analysis. Our method is based on micro-xCT imaging and characterization to obtain a realistic geometry of microstructure and, coupled with indentation tests to recover specific mechanical properties of inclusion and matrix, is used to define mechanical response. Thus, the current modeling method and results of the simulation provide a foundation for subsequent analysis of micromechanical behavior, including the deformation and failure mechanisms of rock-like materials or any other DIANE material. The method can also be employed to model the effects of material and geometry at the microstructural level on macroscopic material strength and behavior under various loading conditions. Moreover, it can be used in the development of new constitutive models and the verification of existing numerical models.

However, these results must be combined with data gleaned by more conventional methods, both at the macroscale and the microscale [Tsafnat et al., 2011]. Some limitations of this method should be mentioned. First, since geometry and microstructural information on coal are collected by micro-xCT, the size of coal sample should be suitable for micro-xCT imaging. So this method may not be suitable for the analysis of mechanical behavior of rock masses or for large samples which cannot be scanned by xCT. Second, the assignment of material properties is somewhat subjective since the thresholds for different materials in the xCT images are based on qualitative thresholds. To overcome this limitation, more scanning and analysis on a large number of samples with different mineral inclusions will be required to achieve optimum thresholds for each material. Third, the mechanical properties of different component materials are difficult to determine by conventional test methods [Tang et al., 2000]. Thus, some properties and related constitutive models have to be assumed, which result in inaccuracies in the evaluation of macroscale behavior.

4. Conclusions

The objective of this work is to quantify the deformation response, including the initiation and evolution of failure behavior in brittle coal. A novel approach is introduced to combine micro-xCT imaging with

mechanical analysis for the deformation and failure of samples. This allows us not only to create detailed, high-resolution models of coal samples but also to assess the evolving 3-D deformation and stress distribution for the entire loading cycle. The following main conclusions are summarized as

1. Incremental analysis of failure reveals that heterogeneity of the specimens affects the evolution and distribution of stress and deformation.
2. The numerical results indicate that shear failure modes dominate prior to peak strength. In contrast, tensile failure is the controlling mechanism postpeak strength.
3. The distribution of the inclusions results in the complexity of the failure of sample.
4. With an increase in the strain rate, a higher proportion of inclusions are driven to failure in the coal. The compressive strength of the coal is strain rate dependent. Compressive strength increases with an increase in the strain rate—as observed in nature.
5. Based on the results of the simulation, an empirical relationship is proposed to describe the relationship between coal strength and strain rate for the range of 10^{-3} to 10^{-2} s^{-1} . The method can be used in the development of new constitutive models and in the application of existing numerical models.

Acknowledgments

The results presented in this article rely on the data collected at State Key Laboratory of Coal Resources and Safe Mining, China University of Mining and Technology Beijing. Data are available for free to external users upon request. However, external users shall acknowledge the source and authors in any publication that makes use of the presented data. The research was financially supported by the Major State Basic Research Development Program fund (grants 2010CB226801 and 2010CB226804), the National Natural Science Foundation of China (grant 51174213), the New Century Excellent Talents in Ministry of Education Support Program of China (NCET-10-0775), the State Key Laboratory of Coal Resources and Safe Mining (SKLCSR13KFA01), and the Fundamental Research Funds for the Central Universities and Fund of China Scholarship Council.

References

- ASTM D4543-85 (1985), Standard practice for preparing rock core specimens and determining dimensional and shape tolerances, in *Annual Book of ASTM Standards*, p. 04.08, American Society for Testing and Materials, Philadelphia, Pa.
- D5142-09 (2009), *Standard Test Methods for Proximate Analysis of the Analysis Sample of Coal and Coke by Instrumental Procedures*, ASTM International, West Conshohocken, Pa.
- Esterle, J. S., G. O'Brien, and T. Kojovic (1994), *Influence of coal texture and rank on breakage energy and resulting size distributions in Australian coals*, in: *6th Australian Coal Science Conference*, pp. 175–181, Australian Inst. Energy, Newcastle, Newcastle, Australia.
- Esterle, J. S., Y. Kolatschek, and G. O'Brien (2002), Relationship between in situ coal stratigraphy and particle size and composition after breakage in bituminous coals, *Int. J. Coal Geol.*, *49*, 195–214.
- Fang, Z., and J. P. Harrison (2002), Development of a local degradation approach to the modelling of brittle fracture in heterogeneous rocks, *Int. J. Rock Mech. Min. Sci.*, *39*, 443–457.
- Feng, X. T., P. Z. Pan, and H. Zhou (2006), Simulation of the rock microfracturing process under uniaxial compression using an elasto-plastic cellular automaton, *Int. J. Rock Mech. Min. Sci.*, *43*, 1091–1108.
- Fuenkajorn, K., and N. Kenkhunthod (2010), Influence of Loading Rate on Deformability and Compressive Strength of Three Thai Sandstones, *Geotech. Geol. Eng.*, *28*, 707–715.
- Garboczi, E., D. P. Bentz, and N. S. Martys (1999), Digital images and computer modeling, in *Experimental Methods in the Physical Sciences*, edited by P. Wong, pp. 1–41, Academic Press.
- Golab, A., C. R. Ward, A. Permana, P. Lennox, and P. Botha (2013), High-resolution three-dimensional imaging of coal using microfocus X-ray computed tomography, with special reference to modes of mineral occurrence, *Int. J. Coal Geol.*, *113*, 97–108.
- Golchert, D., R. Moreno, M. Ghadiri, and J. Litster (2004), Effect of granule morphology on breakage behaviour during compression, *Powder Technol.*, *143-144*, 84–96.
- Gong, F. Q., and G. F. Zhao (2013), Dynamic Indirect Tensile Strength of Sandstone Under Different Loading Rates, *Rock Mech. Rock Eng.*, doi:10.1007/s00603-013-0503-7.
- Hashiba, K., S. Okubo, and K. Fukui (2006), A new testing method for investigating the loading rate dependency of peak and residual rock strength, *Int. J. Rock Mech. Min. Sci.*, *43*, 894–904.
- He, M. C., C. G. Wang, J. L. Feng, D. J. Li, and G. Y. Zhang (2010), Experimental investigations on gas desorption and transport in stressed coal under isothermal conditions, *Int. J. Coal Geol.*, *83*, 377–386.
- Hudson, J. A., and J. Harrison (1997), *Engineering Rock Mechanics-An Introduction to the Principles*, Pergamon, Oxford.
- Ishizuka, Y., H. Koyama, and S. Komura (1993), Effect of strain rate on strength and frequency dependence of fatigue failure of rocks, in *Assessment and Prevention of Failure Phenomena in Rock Engineering*, edited by A. G. Pasamehmetoglu et al., pp. 321–327, A. A. Balkema, Rotterdam.
- Jia, X., and R. A. Williams (2006), From microstructures of tablets and granules to their dissolution behaviors, *Dissolution Technol.*, *13*, 11–19.
- Jia, X., and R. A. Williams (2007), A Hybrid Mesoscale Modelling Approach to Dissolution of Granules and Tablets, *Chem. Eng. Res. Des.*, *85*, 1027–1038.
- Karacan, C. O. (2003), An effective method for resolving spatial distribution of adsorption kinetics in heterogeneous porous media, application for carbon dioxide sequestration in coal, *Chem. Eng. Sci.*, *58*, 4681–4693.
- Karacan, C. O. (2007), Swelling-induced volumetric strains internal to a stressed coal associated with CO₂ sorption, *Int. J. Coal Geol.*, *72*, 209–220.
- Karacan, C. O., and E. Okandan (2000), Fracture cleat analysis of coals from Zonguldak Basin northwestern Turkey relative to the potential of coalbed methane production, *Int. J. Coal Geol.*, *44*, 109–125.
- Karacan, C. O., and E. Okandan (2001), Adsorption and gas transport in coal microstructure: Investigation and evaluation by quantitative X-ray CT imaging, *Fuel*, *80*, 509–520.
- Karacan, C. O., and G. D. Mitchell (2003), Behavior and effect of different coal microlithotypes during gas transport for carbon dioxide sequestration into coal seams, *Int. J. Coal Geol.*, *53*, 201–217.
- Karpyn, Z. T., and M. Piri (2007), Prediction of fluid occupancy in fractures using network modeling and X-Ray microtomography. I: Data conditioning and model description, *Phys. Rev. E*, *76*, 016315, 1–13.
- Kohmura, Y., and Y. Inada (2006), The effect of the loading rate on stress-strain characteristics of tuff, *J. Soc. Mater. Sci.*, *55*, 323–328.
- Kumar, H. (2010), *Inducing Fractures and Cleat Aperture Enhancement in Bituminous Coal via the Application of Microwave Energy Applied*, The Pennsylvania State University, University Park, Pa.
- Li, Y., and C. Xia (2000), Time-dependent tests on intact rocks in uniaxial compression, *Int. J. Rock Mech. Min. Sci.*, *37*, 467–475.

- Lin, C. L., and J. D. Miller (2004), Pore structure of particles beds for fluid transport simulation during filtration, *Int. J. Min. Process.*, *73*, 281–294.
- Ma, G. W., X. J. Wang, and F. Ren (2011), Numerical simulation of compressive failure of heterogeneous rock-like materials using SPH method, *Int. J. Rock Mech. Min. Sci.*, *48*, 353–363.
- Mahabadi, O. K., N. X. Randall, Z. Zong, and G. Grasselli (2012), A novel approach for micro-scale characterization and modelling of geo-materials incorporating actual material heterogeneity, *Geophys. Res. Lett.*, *39*, L01303, doi:10.1029/2011GL050411.
- Mark, C., and T. M. Barton (1996), A new look at the uniaxial compressive strength of coal, in *The 2nd North American Rock Mechanics Symposium*, pp. 405–412, Balkema, Rotterdam, Netherlands.
- Mathews, J. P., J. D. N. Pone, G. D. Mitchell, and P. Halleck (2011), High-resolution X-ray computed tomography observations of the thermal drying of lump-sized subbituminous coal, *Fuel Process. Technol.*, *92*, 58–64.
- Mazumder, S., K.-H. A. Wolf, K. Elewaut, and R. Ephraim (2006), Application of X-ray computed tomography for analyzing cleat spacing and cleat aperture in coal samples, *Int. J. Coal Geol.*, *68*, 205–222.
- Medhurst, T. P. (1996), *Estimation of the in Situ Strength and Deformability of Coal for Engineering Design*, University of Queensland, Brisbane, Australia.
- Medhurst, T. P., and E. T. Brown (1998), A study of the mechanical behaviour of coal for pillar design, *Int. J. Rock Mech. Min. Sci.*, *35*, 1087–1105.
- Okubo, S., Y. Nishimatsu, C. He, and S. Y. Chu (1992), Loading rate dependency of uniaxial compressive strength of rock under water-saturated condition, *J. Soc. Mater. Sci.*, *41*, 403–409.
- Okubo, S., K. Fukui, and Q. Qi (2006), Uniaxial compression and tension tests of anthracite and loading rate dependence of peak strength, *Int. J. Coal Geol.*, *68*, 196–204.
- Olson, J. F., and D. H. Rothman (1997), Two-fluid flow in sedimentary rock: simulation, transport and complexity, *J. Fluid Mech.*, *341*, 343–370.
- Pan, J., Z. Meng, Q. Hou, Y. Ju, and Y. Cao (2013), Coal strength and Young's modulus related to coal rank, compressional velocity and maceral composition, *J. Struct. Geol.*, *54*, 129–135, doi:10.1016/j.jsg.2013.07.008.
- Pone, J. D. N., M. Hile, P. M. Halleck, and J. P. Mathews (2009), Three-dimensional carbon dioxide-induced strain distribution within a confined bituminous coal, *Int. J. Coal Geol.*, *77*, 103–108.
- Pone, J. D. N., P. M. Halleck, and J. P. Mathews (2010), 3D characterization of coal strains induced by compression, carbon dioxide sorption, and desorption at in-situ stress conditions, *Int. J. Coal Geol.*, *82*, 262–268.
- Poulsen, B. A., and D. P. Adhikary (2013), A numerical study of the scale effect in coal strength, *Int. J. Rock Mech. Min. Sci.*, *63*, 62–71.
- Pyrak-Nolte, I. J., C. D. Montemagno, and D. D. Nolte (1997), Volumetric imaging of aperture distributions in connected fracture networks, *Geophys. Res. Lett.*, *24*, 2343–2346, doi:10.1029/97GL02057.
- Randall, N. X., M. Vandamme, and F. J. Ulm (2009), Nanoindentation analysis as a two-dimensional tool for mapping the mechanical properties of complex surfaces, *J. Mater. Res.*, *24*, 679–690.
- Ray, S. K., K. Sarkar, and T. N. Singh (1999), Effect of cyclic loading and strain rate on the mechanical behaviour of sandstone, *Int. J. Rock Mech. Min. Sci.*, *36*, 543–549.
- Scholtès, L., F.-V. Donze, and M. Khanal (2011), Scale effects on strength of geomaterials, case study: Coal, *J. Mech. Phys. Solids*, *59*, 1131–1146.
- Selomulya, C., X. Jia, and R. A. Williams (2005), Direct prediction of structure and permeability of flocculated structures and sediments using 3D tomographic imaging, *Chem. Eng. Res. Des.*, *83*, 844–852.
- Simons, F. J., F. Verhelst, and R. Swennen (1997), Quantitative characterization of coal by means of microfocus X-ray computed microtomography (CMT) and color image analysis (CIA), *Int. J. Coal Geol.*, *34*, 69–88.
- Sleep, N. H. (1997), Application of a unified rate and state friction theory to the mechanics of fault zones with strain localization, *J. Geophys. Res.*, *102*, 2875–2895, doi:10.1029/96JB03410.
- Spanne, P., J. Thovert, C. Jacquin, W. Lindquist, K. Jones, and P. Adler (1994), Synchrotron computed microtomography of porous media—Topology and transports, *Phys. Rev. Lett.*, *73*, 2001–2004.
- Sukop, M. C., H. Huang, C. L. Lin, M. D. Deo, K. Oh, and J. D. Miller (2008), Distribution of multiphase fluids in porous media: Comparison between lattice Boltzmann modeling and micro-x-ray tomography, *Phys. Rev. E*, *77*, 026710.
- Tang, C. A., H. Liu, P. K. K. Lee, Y. Tsui, and L. G. Tham (2000), Numerical studies of the influence of microstructure on rock failure in uniaxial compression—Part I: effect of heterogeneity, *Int. J. Rock Mech. Min. Sci.*, *37*, 555–569.
- Tsafnat, N., G. Tsafnat, and A. S. Jones (2008), Micro-finite element modelling of coke blends using X-ray microtomography, *Fuel*, *87*, 2983–2987.
- Tsafnat, N., N. Amanat, and A. S. Jones (2011), Analysis of coke under compressive loading, A combined approach using micro-computed tomography, finite element analysis, and empirical models of porous structures, *Fuel*, *90*, 384–388.
- Van Geet, M., and R. Swennen (2001), Quantitative 3D-fracture analysis by means of microfocus X-ray computer tomography (μ CT): An example from coal, *Geophys. Res. Lett.*, *28*, 3333–3336, doi:10.1029/2001GL013247.
- Van Geet, M., R. Swennen, and P. David (2001), Quantitative coal characterisation by means of microfocus X-ray computer tomography, colour image analysis and back-scattered scanning electron microscopy, *Int. J. Coal Geol.*, *46*, 11–25.
- Verhelst, F., P. David, W. Fermont, L. Jegers, and A. Vervoort (1996), Correlation of 3D-computerized tomographic scans and 2D-colour image analysis of Westphalian coal by means of multivariate statistics, *Int. J. Coal Geol.*, *29*, 1–21.
- Vogel, H.-J., I. Cousin, O. Ippisch, and P. Bastian (2005), The dominant role of structure for solute transport in soil: Experimental evidence and modelling of structure and transport in a field experiment, *Hydrol. Earth Syst. Sci. Discuss.*, *2*, 2153–2181.
- Wang, G., Y. Cheng, and H. Liang (2003), A new method to determine the formation mechanical properties with cuttings microhardness, *Preroleum Drilling Tech.*, *31*, 7–9.
- Wang, S., D. Elsworth, and J. Liu (2013), Mechanical behavior of methane infiltrated coal: the roles of gas desorption, stress level and loading rate, *Rock Mech. Rock Eng.*, *46*, 945–958.
- Wolf, K.-H. A. A., F. van Bergen, R. Ephraim, and H. Pagnier (2008), Determination of the cleat angle distribution of the RECO-POL coal seams, using CT-scans and image analysis on drilling cuttings and coal blocks, *Int. J. Coal Geol.*, *73*, 259–272.
- Yao, Y. (2009), Non-destructive characterization of coal samples from China using microfocus X-ray computed tomography, *Int. J. Coal Geol.*, *80*, 113–123.
- Zhao, H., and Y. Zhao (2011), An automatic loading system for rock core testing with an industrial CT scanner, *Pet. Sci.*, *8*, 490–493.
- Zhao, Y., and Y. Jiang (2010), Acoustic emission and thermal infrared precursors associated with bump-prone coal failure, *Int. J. Coal Geol.*, *83*, 11–20.
- Zhao, Y., G.-F. Zhao, and Y. Jiang (2013), Experimental and numerical modelling investigation on fracturing in coal under impact loads, *Int. J. Fract.*, *183*, 63–80.